

# A library of *ab initio* Raman spectra for automated identification of 2D materials

Alireza Taghizadeh<sup>†1,2,3</sup>, Ulrik Leffers<sup>3</sup>, Thomas G. Pedersen<sup>1,2</sup>, and Kristian S. Thygesen<sup>3,4</sup>

<sup>1</sup>Department of Materials and Production, Aalborg University, 9220 Aalborg Øst, Denmark

<sup>2</sup>Center for Nanostructured Graphene (CNG), 9220 Aalborg Øst, Denmark

<sup>3</sup>Computational Atomic-scale Materials Design (CAMD), Department of Physics, Technical University of Denmark (DTU), 2800 Kgs. Lyngby, Denmark

<sup>4</sup>Center for Nanostructured Graphene (CNG), Technical University of Denmark (DTU), 2800 Kgs. Lyngby, Denmark

December 21, 2024

## Abstract

Raman spectroscopy is frequently used to identify composition, structure and layer thickness of two-dimensional (2D) materials. Here, we describe an efficient first-principles workflow for calculating Raman spectra of solids and molecules within third-order perturbation theory. The method is used to obtain the Raman spectra of 733 different 2D crystals selected as the most stable materials from the computational 2D materials database (C2DB). The calculations are based on an efficient density functional theory (DFT) implementation employing a localized atomic orbital (LCAO) basis set. We benchmark the computational scheme against available experimental data and present several examples from the database including the evolution of Raman spectra from MoSe<sub>2</sub> over MoSSe to MoS<sub>2</sub>. Furthermore, we propose an automatic procedure for identifying a material based on an input experimental Raman spectrum and illustrate it for the cases of MoS<sub>2</sub> (H-phase) and WTe<sub>2</sub> (T'-phase). The Raman spectra of all materials at three commonly used laser excitation frequencies and nine polarization configurations are freely available from the C2DB where they can be browsed or downloaded as data files. Our work provides a comprehensive and easily accessible library of *ab initio* Raman spectra and should be a valuable information source for both theoreticians and experimentalists in the field of 2D materials.

Following the discovery of graphene in 2004 [1], the field of two-dimensional (2D) materials has grown exponentially during the last decade. Today, more than 50 different monolayer compounds including metals [2, 3], semiconductors [4–7], insulators [8], ferromagnets [9], and superconductors [10, 11], have been chemically grown or mechanically exfoliated from layered bulk crystals [12]. The enormous interest in 2D materials has mainly been driven by their unique and easily tunable properties (as compared to 3D bulk crystals), which make them attractive for both fundamental research and technological applications in areas such as energy conversion/storage, (opto)-electronics, and photonics [7, 13–15]. Among the various experimental techniques used for characterizing 2D materials, Raman spectroscopy plays a pivotal role [16] thanks to its simplicity, non-destructive nature, and high sensitivity towards key materials properties such as chemical composition, layer thickness (number of layers), inter-layer coupling, crystal symmetries, sample quality, etc [17, 18].

Raman spectroscopy is a versatile technique for probing the vibrational modes of molecules and crystals from inelastically scattered light, and is widely used for identifying materials through their unique vibrational fingerprints [19]. When a photon with frequency  $\omega_i$  is incident on a crystal, it can scatter into a different state. The scattered photon may have different frequency, polarization, and direction compared to the incident photon, see Fig. 1(a). In the Rayleigh (elastic) scattering processes, the frequency of the scattered photon,  $\omega_o$ , is the same as the incident one,  $\omega_o = \omega_i$ . In contrast, in

---

<sup>†</sup>ata@nano.aau.dk

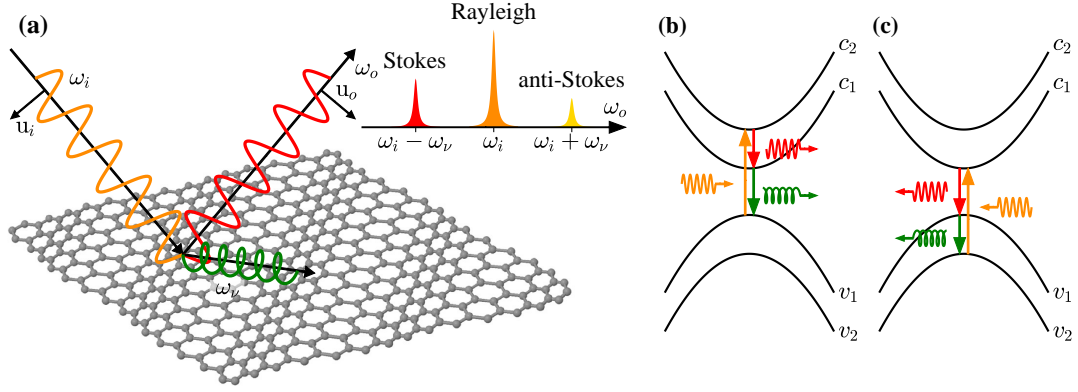


Figure 1: (a) Schematic of Raman scattering processes, in which incident photons of polarization  $\mathbf{u}_i$  and frequency  $\omega_i$  are scattered into  $\mathbf{u}_o$  and  $\omega_o$  under emission (or absorption) of a phonon with frequency  $\omega_\nu$ . In a typical output spectrum, the Rayleigh (elastic), Stokes and anti-Stokes lines are observed. Two types of vertical transitions contribute to the Raman response: (b) two conduction band states with one valence state or (c) two valence states with only one conduction band state, see Eq. (7). The orange, red and green arrows depict the transitions due to electrons interacting with incident photons, scattered photons and phonons, respectively.

the Raman (inelastic) processes, scattering may generate photons at frequencies of  $\omega_i \pm \omega_\nu$ , where  $\omega_\nu$  is the frequency of a (Raman active) vibrational mode of the crystal, i.e. a phonon. In the radiation spectrum, the resonances at  $\omega_i - \omega_\nu$  are referred to as the Stokes bands, while peaks at  $\omega_i + \omega_\nu$  form the anti-Stokes bands, see Fig. 1(a). Depending on the symmetry of the phonon modes and polarization of the electromagnetic fields, a phonon mode may be active or inactive in the Raman spectrum.

While semi-classical theories of Raman spectroscopy can provide some qualitative insight [19], a full quantum mechanical treatment is necessary for a quantitatively accurate description. In particular, *ab initio* techniques have been employed successfully to calculate Raman spectra of both molecules [19, 20] and solids [21–23] typically showing good agreement with experimental spectra. The parameter-free nature of such computational schemes endow them with a high degree of predictive power, although their computational cost can be significant, thus, in practice limiting them to relatively simple, i.e. crystalline, materials. In the realm of 2D materials, *ab initio* Raman studies have been limited to a handful of the most popular 2D crystals including graphene [24], hBN [25], WTe<sub>2</sub> [26], MoS<sub>2</sub> and WS<sub>2</sub> [27]. In view of the significant experimental efforts currently being devoted to the synthesis and application of new 2D materials and the important role of Raman spectroscopy as a main characterization tool, it is clear that the compilation of a comprehensive library of Raman spectra of 2D materials across different crystal structures and chemical compositions is a critical and timely endeavour.

Recently, we have introduced the open Computational 2D Materials Database (C2DB) [12], which contains various calculated properties for several thousands 2D crystals using state of the art *ab initio* methods. The properties currently provided in the C2DB include the relaxed crystal structures, thermodynamic phase diagrams (convex hull), electronic band structures and related quantities (effective masses, deformation potentials, etc.), elastic properties (stiffness tensors, phonon frequencies), and optical conductivity/absorbance spectra. We stress that the materials in the C2DB comprise both experimentally known as well as hypothetical but dynamically stable materials, i.e. materials that are predicted to be stable but may or may not be possible to synthesise in reality.

In this paper, we present an *ab initio* high-throughput computation of the Raman spectra of more than 700 monolayers from the C2DB. The calculations are based on an efficient density functional theory (DFT) implementation of the third order Raman process employing a localized atomic orbital (LCAO) basis set [28]. We describe the implementation and the automated workflow for computing the Raman spectra at three different excitation frequencies and nine polarization setups. All calculated Raman spectra are provided in the Supplementary Information and can be found at the C2DB website [29]. In addition, the applied computational routines are freely available online through the website. Our numerical results are benchmarked against available experimental data for selected 2D crystals such as MoS<sub>2</sub>, MoSSe and MoSe<sub>2</sub>. The calculated spectra show excellent agreement with experiments for the Raman peak positions and acceptable agreement for the relative peak intensities. Finally, we analyze the inverse problem of identifying a material based on an input (experimental) Raman spectrum. Using MoS<sub>2</sub>

(H-phase) and WTe<sub>2</sub> (T'-phase) as two examples, we find that a simple descriptor consisting of the first and second moments of the Raman spectrum combined with the Euclidean distance measure suffices to identify the correct material among the 700+ candidate materials in the database. In particular, this procedure can be used to differentiate clearly the distinct structural phases of MoS<sub>2</sub> and WTe<sub>2</sub>. Incidentally, the library of calculated Raman spectra provides a useful dataset for training machine learning algorithms [30, 31]. As such, our work is not only a valuable reference for experimentalists and theoreticians working in the field of 2D materials, but also represents a step in the direction of autonomous (in-situ) characterization of materials.

## 1 Raman scattering

We first briefly review the theory of Raman scattering in the context of third-order perturbation theory. As discussed above, accurate modeling of Raman processes requires a quantum mechanical treatment to obtain the electronic properties. Regarding the electromagnetic field, it can be shown that a classical description of the field [32, 33] yields the same results as the full quantum mechanical theory that quantizes the photon field [19, 34, 35]. The most common approach to Raman calculations is the Kramers-Heisenberg-Dirac approach, [33] in which the Raman tensor is obtained as a derivative of the electric polarizability with respect to the vibrational normal modes [21, 27, 32, 33, 36]. Nonetheless, here we employ a more direct and much less explored approach based on time-dependent third-order perturbation theory to obtain the rate for coherent electronic processes involving creation/annihilation of two photons and one phonon. While the two approaches can be shown to be equivalent [19], at least when local field effects can be ignored as is the case for 2D materials, the third-order perturbative approach can be readily extended to higher order Raman processes (e.g. scattering on multiple phonons), and provides a more transparent physical picture of the Raman processes in terms of individual scattering events [37]. Hence, our computational framework is prepared for future extensions to multi-phonon processes. Note that in terms of computational effort, the perturbative approach is comparable to the polarizability derivative method for typical crystals, for which the matrix element calculation dominates the computation time. In this case, both approaches scale as  $N_\nu N_b^2$ , where  $N_\nu$  and  $N_b$  denote the number of phonon modes and electronic bands, respectively.

To derive an expression for the Raman intensity, both electron-light ( $\hat{H}_{e\gamma}$ ) and electron-phonon ( $\hat{H}_{e\nu}$ ) Hamiltonians are treated as perturbations written as  $\hat{H}_{e\gamma} + \hat{H}_{e\nu} \equiv \sum_\omega \hat{H}'(\omega) \exp(-i\omega t)$  ( $\omega$  runs over positive and negative frequencies and can also be zero for electron-phonon coupling). The exact form of these Hamiltonians is given in the method section. Within third-order perturbation theory, the transition rate  $P_{i \rightarrow f}^{(3)}$  from an initial state  $|\psi_i\rangle$  to a final state  $|\psi_f\rangle$  due to the perturbative Hamiltonian  $\hat{H}_{e\gamma} + \hat{H}_{e\nu}$ , is given by [38]

$$P_{i \rightarrow f}^{(3)} = \frac{2\pi}{\hbar} \left| \sum_{ab} \sum_{\omega_1 \omega_2 \omega_3} \frac{\langle \psi_f | \hat{H}'(\omega_1) | \psi_a \rangle \langle \psi_a | \hat{H}'(\omega_2) | \psi_b \rangle \langle \psi_b | \hat{H}'(\omega_3) | \psi_i \rangle}{(E_i - E_a + \hbar\omega_2 + \hbar\omega_3)(E_i - E_b + \hbar\omega_3)} \right|^2 \times \delta(E_f - E_i - \hbar\omega_1 - \hbar\omega_2 - \hbar\omega_3). \quad (1)$$

Here,  $a, b$  summations are performed over all intermediate states, and the Dirac delta ensures energy conservation. The intensity  $I(\omega)$  of the Stokes Raman process for a phonon mode  $\nu$  is proportional to  $P_{i \rightarrow f}^{(3)}$ , when the initial and final states of the system are given by  $|\psi_i\rangle = |0\rangle \otimes |n_\nu\rangle$  and  $|\psi_f\rangle = |0\rangle \otimes |n_\nu + 1\rangle$ , respectively [35]. Here,  $|0\rangle$  denotes the ground state of the electronic system and  $|n_\nu\rangle$  is a state with  $n_\nu$  phonons at frequency of  $\omega_\nu$ . The transition rate corresponding to the Stokes process involves a photon absorption, followed by an emission of a single phonon and photon [39], i.e.  $(\omega_1, \omega_2, \omega_3) = \mathcal{P}(-\omega_i, \omega_o, 0)$  with  $\mathcal{P}$  indicating all possible permutations of the arguments (six terms in total).

We assume a time-harmonic field given by  $\mathcal{E}(t) = \mathcal{E}_i \mathbf{u}_i \exp(-i\omega_i t) + \mathcal{E}_o \mathbf{u}_o \exp(-i\omega_o t) + \text{complex conjugate}$ , where  $\mathcal{E}_{i,o}$  and  $\omega_{i,o}$  are the amplitudes and frequencies of the input/output electromagnetic fields, respectively, see Fig. 1(a). In addition,  $\mathbf{u}_{i,o} = u_{i,o}^x \mathbf{e}_x + u_{i,o}^y \mathbf{e}_y + u_{i,o}^z \mathbf{e}_z$  denote the corresponding polarization vectors, where  $\mathbf{e}_\alpha$  is the unit vector along the  $\alpha$ -direction with  $\alpha = x, y, z$ . Inserting the Hamiltonians, i.e. Eq. (6) in Eq. (1), the expression for the Stokes Raman intensity involving scattering events by only one phonon can be written

$$I(\omega) = C_0 \sum_\nu \frac{n_\nu + 1}{\omega_\nu} \left| \sum_{\alpha\beta} u_i^\alpha R_{\alpha\beta}^\nu u_o^\beta \right|^2 \delta(\omega - \omega_\nu). \quad (2)$$

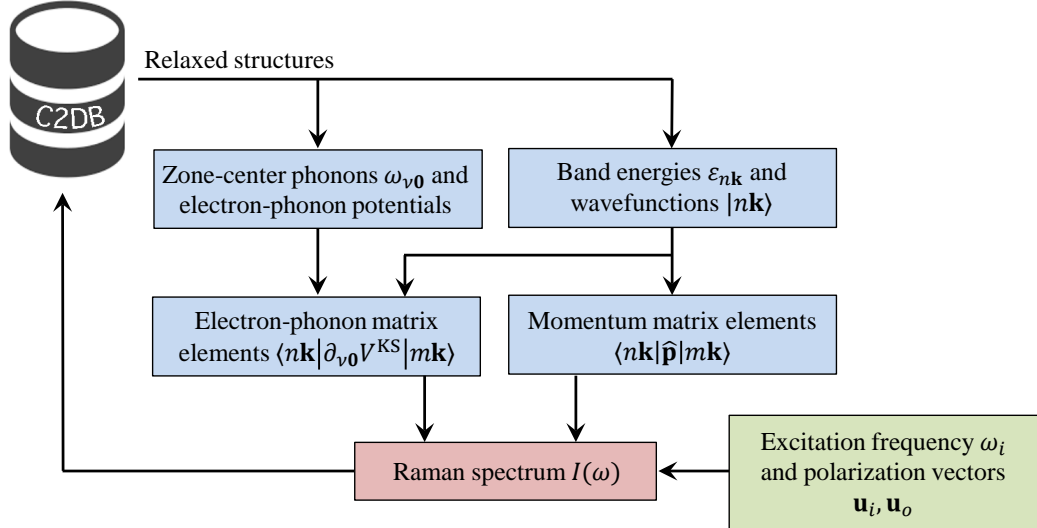


Figure 2: Diagram of the steps necessary to calculate the Raman tensor of a material. First, the relaxed structures are extracted from the C2DB. Next, the electron-phonon coupling terms and the momentum matrix elements are evaluated. Finally, the Raman spectrum is evaluated for a given excitation frequency and polarization configuration and the results are stored in the database, see method section for notation.

Here,  $C_0$  is an unimportant constant, and  $n_\nu$  is given by the Bose–Einstein distribution, i.e.  $n_\nu \equiv (\exp[\hbar\omega_\nu/k_B T] - 1)^{-1}$  at temperature  $T$ . Due to momentum conservation, only phonons at the center of the Brillouin zone contribute to the one-phonon Raman processes. Furthermore,  $R_{\alpha\beta}^\nu$  denotes the Raman tensor for phonon mode  $\nu$ , see method section. Similarly to other third-order processes, the Raman tensor has contributions from two different types of transitions as shown in Figs. 1(b) and 1(c), which involve one/two empty states with two/one filled state. Equation (2) is used for computing the Raman spectra in this work for a given excitation frequency and polarization setup. It may be noted that one can derive a similar expression for the anti-Stokes Raman intensity by replacing  $n_\nu + 1$  by  $n_\nu$  in Eq. (2) and  $\omega_\nu$  by  $-\omega_\nu$  in Eq. (7) in method section. Note, also, that the Raman shift  $\hbar\omega$  is expressed in  $\text{cm}^{-1}$  (1 meV is equivalent to  $8.0655 \text{ cm}^{-1}$ ).

## 2 Results and discussion

An overview of the automated workflow for computing the Raman tensor of the materials in the C2DB is shown in Fig. 2. First, the relaxed structures are extracted from the database. Next, the electronic band energies and wave functions are obtained from a DFT calculation. In parallel, a zone-center phonon calculation is performed to obtain the optical vibrational modes. From the obtained electronic states and phonon modes, the momentum and electron-phonon matrix elements are evaluated and stored. In the final step, for a given excitation frequency and input/output polarization vectors, the Raman spectrum is calculated using Eq. (2). The key feature of the approach outlined here is that the calculation process can be automatized, allowing one to perform thousands of calculations in parallel without human intervention.

For simplicity, we have restricted the study to non-magnetic materials, but our routines can be readily extended to include magnetic materials. Except for the cases shown in Figs. 4(b) and 7, the Raman spectra presented in this paper are computed for the in-plane polarization, where the incoming and outgoing photons are polarized along the  $x$ -direction (referred to as the  $xx$  polarization in this work with  $\mathbf{u}_i = \mathbf{u}_o = [1, 0, 0]$ ).

Figure 3 compares the calculated Raman spectrum of three different monolayer TMDs, namely MoSe<sub>2</sub>, MoSSe and MoS<sub>2</sub>, with the experimental data extracted from Ref. [40]. For all three monolayers, a good agreement is observed both for the peak positions and relative amplitudes of the main peaks. Additional peaks in the experimental spectra presumably originate from the substrate or defects in the samples. The differences between the Raman spectra of the three materials provide valuable information about the crystal structure. When one of the selenium atoms in MoSe<sub>2</sub> is replaced with the lighter sulfur atoms

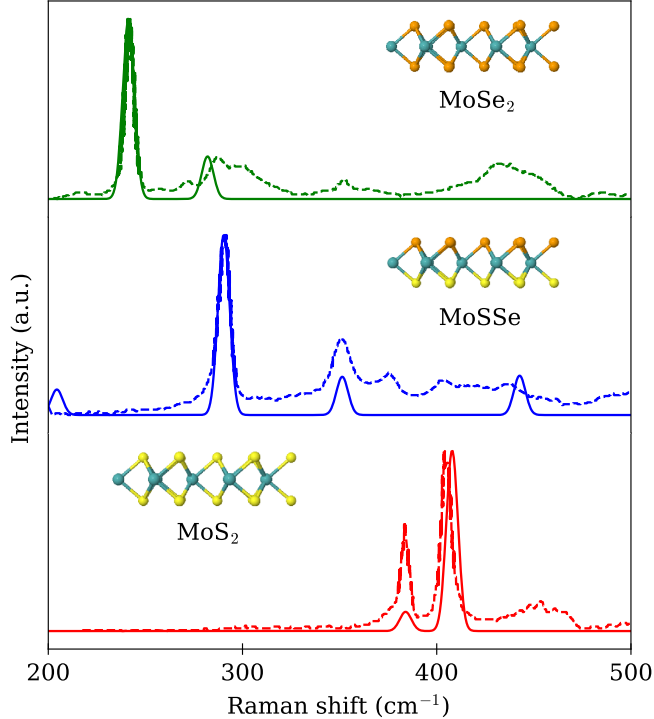


Figure 3: Comparison of the computed Raman spectra (solid) with the experimental results in Ref. [40] (dashed) for MoSe<sub>2</sub> (top), MoSSe (middle) and MoS<sub>2</sub> (bottom). The excitation wavelength is 532 nm, and both input and output electromagnetic fields are polarized along the  $x$ -direction (zigzag direction).

and MoSSe is formed, the energies of the two Raman active modes ( $E'$  and  $A'_1$ ) increase. Furthermore, two new modes appear in the Raman spectrum due to the broken symmetry in the  $z$ -direction. If the remaining layer of selenium is replaced with sulfur atoms, creating a monolayer of MoS<sub>2</sub>, again only two Raman active phonon modes remain but they appear at larger frequencies due to the lighter mass of sulfur atoms compared to selenium.

Next, we focus on the case of MoS<sub>2</sub>, and investigate the dependency of the Raman spectrum on the excitation frequency and polarization, see Figs. 4(a) and 4(b), respectively. In Fig. 4(a), the Raman spectra are computed for three commonly used wavelengths of blue, green and red laser sources. In this case both in- and outgoing polarization vectors are along the  $x$ -direction. While the relative strength of the first Raman active peak in the spectrum is enhanced slightly for shorter wavelengths, the shape of the spectrum does not change significantly. Note that, in reality, the relative amplitudes of the two Raman peaks at 385 cm<sup>-1</sup> and 407 cm<sup>-1</sup> may change considerably if the excitation frequency coincides with an exciton resonance [41, 42]. This is because excitons can selectively enhance specific Raman modes due to their symmetry [43]. Although this effect is not captured properly in our independent-electron model, it is in principle straightforward to include by using the many-body eigenstates obtained by diagonalizing the Bethe-Salpeter equation (BSE) when evaluating the matrix elements in Eq. (1) [44]. Moreover, the absolute magnitudes of the Raman peaks can vary substantially by changing the excitation wavelength due to the possible resonance with electronic states (resonance Raman spectroscopy) [43]. Nonetheless, the overall magnitude of the Raman spectra is usually of little practical importance compared to the spectral positions and spectra are typically normalized as done here. Changing the polarization of electromagnetic fields not only influences the relative amplitudes of Raman peaks, but may switch certain modes on and off as shown in Fig. 4(b). For instance, the MoS<sub>2</sub> Raman peak at 385 cm<sup>-1</sup> becomes completely inactive for the perpendicular polarization setup ( $zz$ ) due to symmetry [27].

To give an impression of the type of data resulting from our high-throughput study, Fig. 5 shows the computed Raman spectra for  $xx$ -polarization at an excitation wavelength of 532 nm for twelve different monolayer crystals (shown in the insets). As expected, the number of peaks in the Raman spectra, i.e. the number of Raman active modes, increases with the number of atoms in the unit cell. For instance, there are more than 10 peaks in the Raman spectrum of CoClO. Furthermore, as a rule of thumb, materials that contain heavier atoms possess Raman peaks at lower frequencies and vice versa, e.g. the

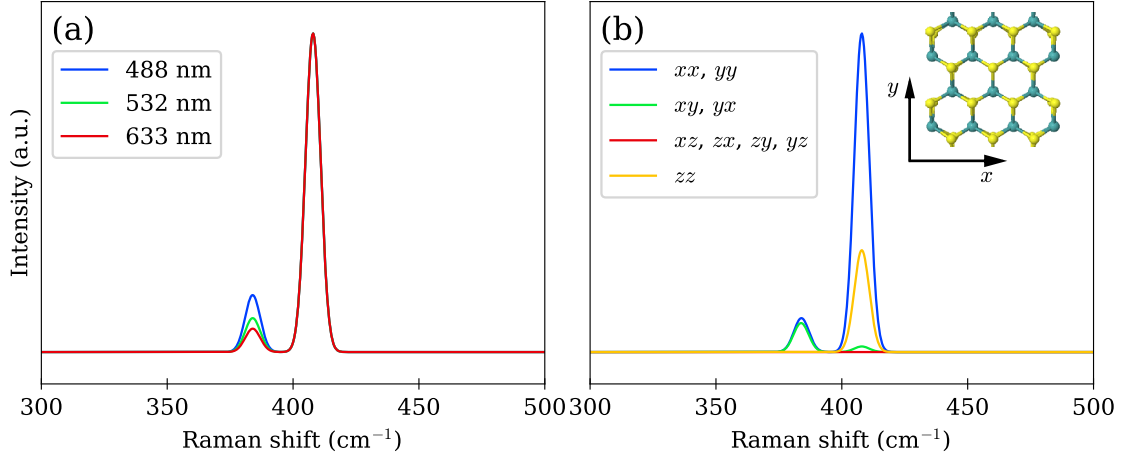


Figure 4: (a) Raman spectra of MoS<sub>2</sub> evaluated at three different excitation wavelengths, blue (488 nm), green (532 nm), and red (633 nm) for the  $xx$ -polarization setup. (b) Polarized Raman spectra of MoS<sub>2</sub> for various input and output polarization directions at 532 nm excitation wavelength. The inset shows a top view of the crystal structure.

Raman peaks for graphene, hBN and CH appear at frequencies above 1000 cm<sup>-1</sup>. There is a good agreement for the main Raman peaks of the calculated spectra in Fig. 5 with the available experimental results for graphene [24], hBN [25], black phosphorus [45], and WTe<sub>2</sub> [46].

At this point, we turn to a critical test of the *ab initio* Raman library: given an experimental Raman spectrum, is it possible to identify the underlying material by comparing the experimental spectrum to a library of calculated spectra? The answer to this question will depend on several factors including: (1) The quality of the experimental spectrum. (2) The quality of the calculated spectra, i.e. the ability of theory to reproduce a (high quality) experimental spectrum for a given material. (3) The size/density of the calculated Raman spectrum database. Obviously, a more densely populated database increases the chances that the experimental sample is, in fact, contained in the database. But, at the same time, this increases the risk of obtaining a false positive, i.e. matching the experimental spectrum by a calculated spectrum of a different material.

Putting the above idea into practice requires a quantitative measure for comparing Raman spectra. In the present work, we use the two lowest moments to fingerprint the Raman spectrum. In general, the  $N^{\text{th}}$  Raman moment of the spectrum is given by

$$\langle \omega^N \rangle \equiv \int_0^\infty I(\omega) \omega^N d\omega = \sum_\nu I_\nu \omega_\nu^N, \quad (3)$$

where,  $I_\nu$  denotes the amplitude of mode  $\nu$ , i.e.  $I_\nu = (n_\nu + 1) |\sum_{\alpha\beta} u_i^\alpha R_{\alpha\beta}^\nu u_o^\beta|^2 / \omega_\nu$ . Note that, for these calculations, we normalize the Raman spectrum such that its zeroth moment becomes one, i.e.  $\int_0^\infty I(\omega) d\omega = \sum_\nu I_\nu = 1$ . Therefore, the first Raman moment corresponds to the mean value of the spectrum. Rather than using the second moment, we use the standard deviation of the spectrum as the selected measure, given by

$$\delta\omega = \sqrt{\langle \omega^2 \rangle - \langle \omega \rangle^2}. \quad (4)$$

Figure 6 shows a scatter plot of  $\langle \omega \rangle$  and  $\delta\omega / \langle \omega \rangle$  for the 733 monolayers at an excitation wavelength of 532 nm and  $xx$  polarization setup obtained at the room temperature. In this plot, crystals composed of lighter elements appear further to the right because their optical phonons generally have higher energies. Furthermore, crystals with fewer atoms in the unit cell and/or higher degree of symmetry, appear in the bottom of the plot because they have fewer (non-degenerate) phonons and thus fewer peaks in their Raman spectrum resulting in a reduced frequency spread. In particular,  $\delta\omega$  vanishes for materials with only a single Raman peak such as graphene and hBN.

To test the feasibility of inverse Raman mapping, we evaluate the lowest Raman moment fingerprint for five experimental Raman spectra of MoS<sub>2</sub> (H-phase) and three spectra of WTe<sub>2</sub> (T'-phase) obtained from independent studies, see stars in Fig. 6. Firstly, note that the fingerprint of MoS<sub>2</sub> in the T'-phase (WTe<sub>2</sub> in H-phase) is located relatively far from the H-phase (T'-phase) fingerprint in the plot, which

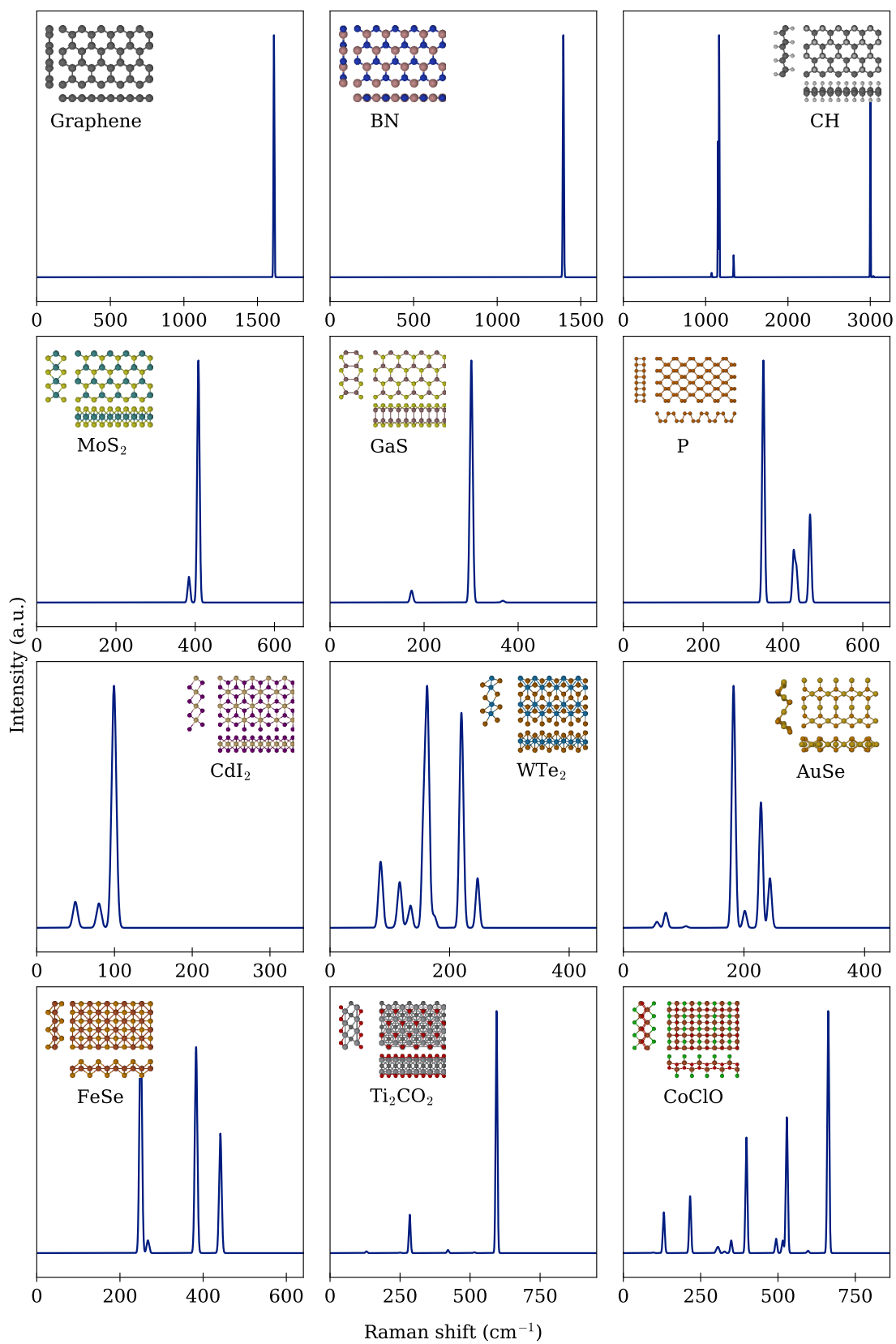


Figure 5: Selection of calculated Raman spectra for twelve different crystal structures currently included in the C2DB. The reduced chemical formulas and schematic cross sectional views of the crystal structures are shown in the insets. The Raman spectra of 733 2D crystals can be found in the Supplementary Information and at the C2DB webpage.

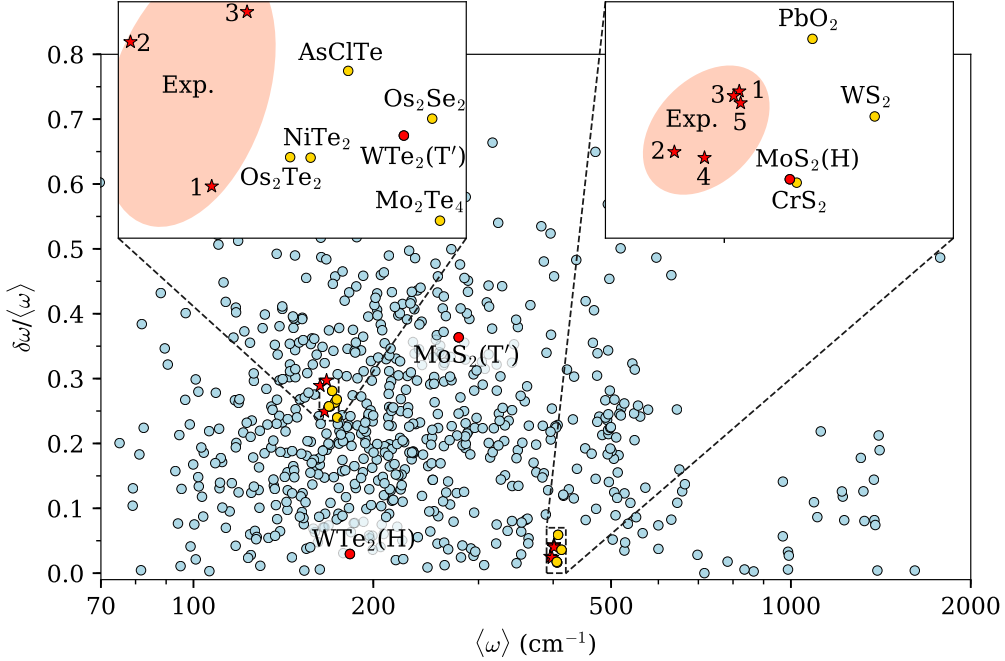


Figure 6: Scatter plot of the first Raman moment and normalized standard deviation for 733 calculated spectra at excitation wavelength of 532 nm and  $xx$  polarization setup (circles). For comparison, several independent experimental spectra for monolayer MoS<sub>2</sub> (in H-phase) and WTe<sub>2</sub> (in T'-phase) are also shown (stars). We highlight the points corresponding to MoS<sub>2</sub> and WTe<sub>2</sub> in red (H-phase, T'-phase, and experiments). The insets are zooms of the vicinity of the experimental data for MoS<sub>2</sub> and WTe<sub>2</sub>. For MoS<sub>2</sub>, 1 to 5 correspond to the experimental spectra obtained from Refs. [40], [47], [48], [49], and [43], respectively, whereas 1 to 3 for WTe<sub>2</sub> are adopted from Refs. [50], [51], and [52], respectively. The calculated Raman fingerprints of both MoS<sub>2</sub> and WTe<sub>2</sub> match well with the experimental data, showing that the simple lowest moment fingerprint suffices to identify the material. In particular, note that the Raman fingerprints of the H- and T'-phases are clearly distinct for both MoS<sub>2</sub> and WTe<sub>2</sub> and, hence, appear in different regions of the plot.

suggests that the lowest Raman moments are indeed able to distinguish different structural phases of the same material. The insets highlight the regions surrounding the experimental data. The variation in the experimental fingerprints is due to small differences in the Raman spectra, originating from the variations in sample quality, substrate effects, measurement techniques/conditions, etc. Consequently, the precise peak positions and, in particular, their amplitudes can vary from one experiment to another. Clearly, the fingerprints of the calculated spectra for both MoS<sub>2</sub> and WTe<sub>2</sub> lie close to the experimental data. In fact, the deviation between theory and experiments is comparable to the variation between the different experiments. Importantly, only a few other materials show a similar agreement with the experimental data. This suggests that fingerprints including higher order moments could single out the correct material with even higher precision. For instance, the skewness (based on the third Raman moment) can be used to distinguish MoS<sub>2</sub> from CrS<sub>2</sub>. By manual inspection of the Raman spectra, one readily confirms that the calculated spectra of MoS<sub>2</sub> and WTe<sub>2</sub> are in fact the best match to the experimental spectra, e.g. other candidates have Raman peaks that are not observed in the experimental spectra or the relative amplitudes of the peaks are completely different from the experimental data. Nonetheless, the procedure of manual inspection can be replaced by a more rigorous and unbiased approach as discussed below.

To compare the experimental and calculated Raman spectra quantitatively, we focus on the experimental data of Refs. [49] and [52] for MoS<sub>2</sub> and WTe<sub>2</sub>, respectively. The experimental spectra for MoS<sub>2</sub> are obtained without any polarizer at 77 K at an excitation wavelength of 488 nm. For WTe<sub>2</sub> in Ref. [52], the experiment is performed at room temperature using a 532 nm laser linearly polarized in-plane. To account for the unspecified polarization, we take the average of Raman spectra for the  $xx$  and  $xy$  polarization setups in the case of WTe<sub>2</sub>, while for MoS<sub>2</sub> the average of all Raman spectra for transverse components ( $xx$ ,  $xy$ ,  $yx$  and  $yy$ ) is used as the theoretical spectrum. For quantitative comparison with the experimental data, one can use Euclidean distances between the experimental and theoretical spectra

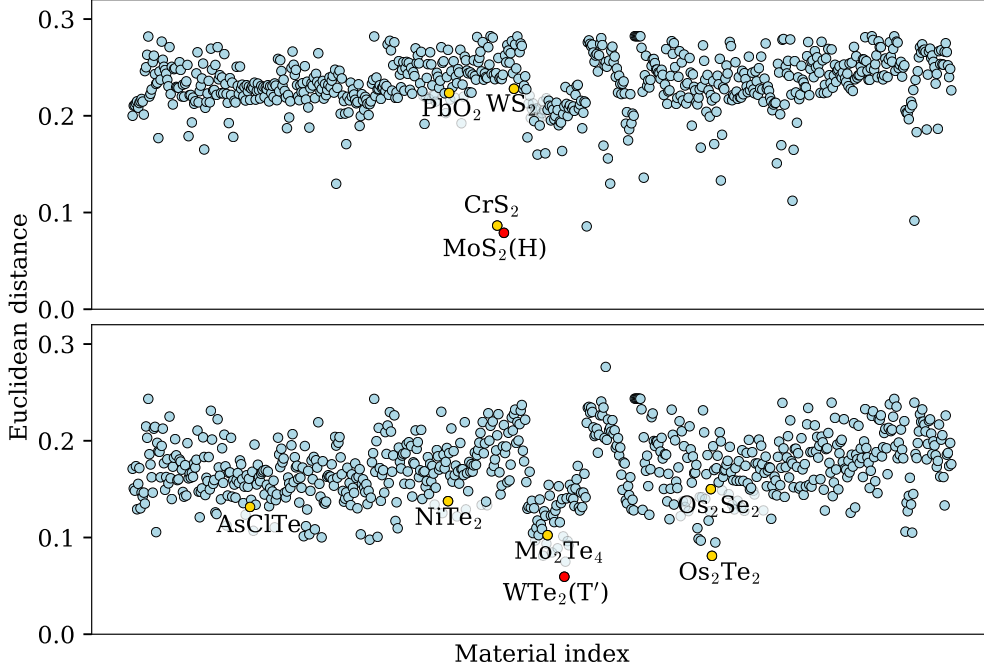


Figure 7: Euclidean distances (see main text for details) between all calculated Raman spectra and the experimental data of Refs. [49] and [52] for MoS<sub>2</sub> (top) and WTe<sub>2</sub> (bottom). For comparison purposes, we highlight the points corresponding to materials in the insets of Fig. 6 by yellow. The theoretical Raman spectra of MoS<sub>2</sub> and WTe<sub>2</sub> (shown in red) are the closest to the measurements and, hence, have the shortest Euclidean distance.

as a measure. For two Raman spectra  $I_1(\omega)$  and  $I_2(\omega)$ , the Euclidean distance (or  $L^2$ -norm)  $\|I_1 - I_2\|$  is defined as

$$\|I_1 - I_2\| \equiv \left( \int_0^\infty |I_1(\omega) - I_2(\omega)|^2 d\omega \right)^{1/2}. \quad (5)$$

Note that the spectra are normalized such that the total area is unity. Figure 7 shows the computed Euclidean distances from the calculated Raman spectra to the experimental data for both MoS<sub>2</sub> and WTe<sub>2</sub>. We highlight the points corresponding to the materials in the insets of Fig. 6. In both cases, identifying the smallest Euclidean distance confirms that the Raman spectra closest to the experimental data are indeed the calculated spectra of MoS<sub>2</sub> and WTe<sub>2</sub>. This shows that the quality and accuracy of, respectively, the experimental and computed 2D materials Raman spectra, is sufficient for automatic structure identification.

### 3 Conclusion and outlook

We have introduced a comprehensive library of *ab initio* computed Raman spectra for more than 700 2D materials spanning a variety of chemical compositions and crystal structures. The 2D materials comprise both experimentally known and hypothetical compounds, all dynamically stable and with low formation energies. Using an efficient first-principles implementation of third-order perturbation theory, the full Raman tensor was calculated including all nine possible combinations for polarization vectors of the input/output photons and three commonly used excitation wavelengths. All spectra are freely available as part of the C2DB and should comprise a valuable reference for both theoreticians and experimentalists in the field. The reliability of the computational approach was demonstrated by comparison with experimental spectra for several monolayer transition metal dichalcogenides.

We carefully tested the feasibility of inverse Raman mapping, i.e. to what extent the library of computed Raman spectra can be used to identify the composition and crystal structure of an unknown material from its Raman spectrum. For the specific cases of MoS<sub>2</sub> in H-phase and WTe<sub>2</sub> in T'-phase, we showed that a simple fingerprint based on the lowest moments of the Raman spectrum is sufficient to identify the materials from their experimental Raman spectrum. This represents a significant step in the direction of autonomous identification/characterization of materials. In addition, apart from being

a useful reference for 2D materials research, the Raman library can be used to train machine learning algorithms to predict Raman spectra directly from the atomic structure similarly to recent work on prediction of linear optical spectra for molecules [53]. This is of particular importance in the currently attractive trend of employing machine learning algorithms in materials science [30, 31, 54].

In the present work, we have focused on Raman processes involving only a single phonon since these are typically the dominant contributions to the Raman spectrum. Nonetheless, the presented methodology can be readily extended to include two-phonon scattering processes, although the computational cost will be significantly increased. Excitonic effects in the Raman spectrum have been neglected since most experimental Raman spectra are recorded off-resonance where excitons play a minor role. The inclusion of excitonic effects can be achieved within the presented methodology by employing the many-body eigenstates obtained from the BSE [55–57] instead of Slater determinantal electron-hole excitations. However, this will mainly affect the amplitude of the Raman peaks which is of secondary importance in practice. We only compute the Raman spectra of monolayers in the present work, but the library can be extended to multi-layer structures by employing an appropriate exchange-correlation functional capable of accurate modeling of van der Waals forces. Finally, the current work has been restricted to non-magnetic materials, and the *ab initio* Raman response of magnetic materials is an interesting future research field.

## 4 Methods

**Theory:** In the independent-particle approximation, the Hamiltonian of a system of electrons interacting with phonons and electromagnetic fields takes the form  $\hat{H} = \hat{H}_0 + \hat{H}_{e\gamma} + \hat{H}_{e\nu}$ , where  $\hat{H}_0$  is the unperturbed Hamiltonian of the electrons ( $e$ ) and phonons ( $\nu$ ),  $\hat{H}_{e\gamma}$  describes the electron-light interaction, and  $\hat{H}_{e\nu}$  describes the electron-phonon coupling. In second quantization, they are given by [58]

$$\hat{H}_0 \equiv \sum_{n\mathbf{k}} \varepsilon_{n\mathbf{k}} \hat{c}_{n\mathbf{k}}^\dagger \hat{c}_{n\mathbf{k}} + \sum_{\nu\mathbf{q}} \hbar\omega_{\nu\mathbf{q}} (\hat{a}_{\nu\mathbf{q}}^\dagger \hat{a}_{\nu\mathbf{q}} + \frac{1}{2}), \quad (6a)$$

$$\hat{H}_{e\gamma}(t) = \sum_{nm\mathbf{k}} h_{nm\mathbf{k}}(t) \hat{c}_{n\mathbf{k}}^\dagger \hat{c}_{m\mathbf{k}}, \quad (6b)$$

$$\hat{H}_{e\nu} = \sum_{nm\nu} \sum_{\mathbf{k}\mathbf{q}} \sqrt{\frac{\hbar}{\omega_{\nu\mathbf{q}}}} g_{nm\mathbf{k}}^{\nu\mathbf{q}} \hat{c}_{n\mathbf{k}}^\dagger \hat{c}_{m\mathbf{k}} (\hat{a}_{\nu\mathbf{q}} + \hat{a}_{\nu(-\mathbf{q})}^\dagger). \quad (6c)$$

Here,  $\hat{c}^\dagger/\hat{c}$  and  $\hat{a}^\dagger/\hat{a}$  are the creation/annihilation operators of electrons and phonons, respectively,  $\varepsilon_{n\mathbf{k}}$  is the energy of the electronic state  $|n\mathbf{k}\rangle$ , and  $\hbar\omega_{\nu\mathbf{q}}$  denotes the phonon energy of normal mode  $\nu$  and wavevector  $\mathbf{q}$ . Furthermore,  $h_{nm\mathbf{k}}(t) = \langle n\mathbf{k}|\mathcal{A}(t) \cdot \mathbf{p}|m\mathbf{k}\rangle/2m$  and  $g_{nm\mathbf{k}}^{\nu\mathbf{q}} = \langle n\mathbf{k} + \mathbf{q}|\partial_{\nu\mathbf{q}} V^{\text{KS}}|m\mathbf{k}\rangle$  are the electron-light interaction (in the velocity gauge [59]) and electron-phonon matrix elements (to the first order in the atomic displacements [58]), respectively, with the vector potential  $\mathcal{A}$  ( $\mathcal{E} = -\partial\mathcal{A}/\partial t$ ) and Kohn-Sham potential  $V^{\text{KS}}$ . The summation over  $\mathbf{k}$  implies an integral over the first Brillouin zone, i.e.  $(2\pi)^D \sum_{\mathbf{k}} \rightarrow V^D \int_{\text{BZ}} d^D\mathbf{k}$  where  $V$  is the  $D$ -dimensional volume ( $D = 2$  for 2D systems). Note that the  $\mathcal{A}^2$  term does not contribute to the linear Raman response and, hence, is absent here. Moreover, we neglect the Coulomb interaction between electrons and holes, i.e. excitonic effects. If the Raman spectroscopy is performed with an excitation frequency that matches the exciton energy [41], i.e. for resonant Raman spectroscopy, the electron-hole interactions should be included, ideally within the GW and BSE framework [44].

**Raman tensor:** The equation for the Raman tensor component,  $R_{\alpha\beta}^\nu$ , reads

$$\begin{aligned} R_{\alpha\beta}^\nu \equiv \sum_{ijmn\mathbf{k}} & \left[ \frac{p_{ij}^\alpha (g_{jm}^\nu \delta_{in} - g_{ni}^\nu \delta_{jm}) p_{mn}^\beta}{(\hbar\omega_i - \varepsilon_{ji})(\hbar\omega_o - \varepsilon_{mn})} + \frac{p_{ij}^\alpha (p_{jm}^\beta \delta_{in} - p_{ni}^\beta \delta_{jm}) g_{mn}^\nu}{(\hbar\omega_i - \varepsilon_{ji})(\hbar\omega_\nu - \varepsilon_{mn})} \right. \\ & + \frac{p_{ij}^\beta (g_{jm}^\nu \delta_{in} - g_{ni}^\nu \delta_{jm}) p_{mn}^\alpha}{(-\hbar\omega_o - \varepsilon_{ji})(-\hbar\omega_i - \varepsilon_{mn})} + \frac{p_{ij}^\beta (p_{jm}^\alpha \delta_{in} - p_{ni}^\alpha \delta_{jm}) g_{mn}^\nu}{(-\hbar\omega_o - \varepsilon_{ji})(\hbar\omega_\nu - \varepsilon_{mn})} \\ & \left. + \frac{g_{ij}^\nu (p_{jm}^\alpha \delta_{in} - p_{ni}^\alpha \delta_{jm}) p_{mn}^\beta}{(-\hbar\omega_\nu - \varepsilon_{ji})(\hbar\omega_o - \varepsilon_{mn})} + \frac{g_{ij}^\nu (p_{jm}^\beta \delta_{in} - p_{ni}^\beta \delta_{jm}) p_{mn}^\alpha}{(-\hbar\omega_\nu - \varepsilon_{ji})(-\hbar\omega_i - \varepsilon_{mn})} \right] f_i(1-f_j)f_n(1-f_m), \end{aligned} \quad (7)$$

where  $\omega_\nu \equiv \omega_{\nu\mathbf{0}}$ ,  $\varepsilon_{ij} \equiv \varepsilon_{i\mathbf{k}} - \varepsilon_{j\mathbf{k}}$ ,  $p_{ij}^\alpha \equiv \langle i\mathbf{k}|\hat{p}^\alpha|j\mathbf{k}\rangle$ ,  $g_{ij}^\nu \equiv \langle i\mathbf{k}|\partial_{\nu\mathbf{0}} V^{\text{KS}}|j\mathbf{k}\rangle$ ,  $(i, j, m, n)/\nu$  are the electron/phonon band index,  $\delta_{ij}$  denotes the Kronecker delta, and  $f_i \equiv (1 + \exp[(\varepsilon_{i\mathbf{k}} - \mu)/k_B T])^{-1}$  is

the Fermi-Dirac distribution with chemical potential  $\mu$ . The line-shape broadening is accounted for by adding a small phenomenological imaginary part,  $i\eta$ , to the photon frequencies  $\omega_{i,o} \rightarrow \omega_{i,o} + i\eta$ , and the conservation of energy leads to  $\omega_i = \omega_o + \omega_\nu$ . We set the frequency broadening to  $\eta = 200$  meV in our calculations. Since we are only considering scattering with one phonon, only zone-center phonons contribute due to momentum conservation, i.e. only phonons at  $\mathbf{q} = \mathbf{0}$  are considered. In each of the six terms in Eq. (7), two distinct types of transitions contribute as shown schematically in Figs. 1(b) and 1(c). In the first type, one valence state and two conduction states contribute to the response, whereas in the second type it is one conduction state in combination with two valence states.

**First-principles calculations:** All DFT calculations are performed with the projector augmented wave code, GPAW [60, 61], in combination with the atomic simulation environment (ASE) [62, 63]. The Perdew-Burke-Ernzerhof (PBE) exchange-correlation functional is used [64] and the Kohn-Sham orbitals are expanded using the double zeta polarized (dzp) basis set [28]. The monolayers are placed between two vacuum regions with thicknesses of 15 Å. A convergence test of Raman spectra with respect to the wavevector density is performed for several materials, and a mesh with the density of 25 Å<sup>-1</sup> for ground state calculations was chosen. The phonon modes are obtained using the standard approach based on calculating the dynamical matrices in the harmonic approximation [65, 66]. The dynamical matrix is evaluated using the small-displacement method [67], where the change of forces on a specific atom caused by varying the position of neighbouring atoms is computed. Since only the zone-centered ( $\Gamma$ -point) phonons are required, the phonon modes can be computed based on the crystal unit cell. A k-mesh with a density of 12 Å<sup>-1</sup> is used for phonon calculations, and the forces are converged within 10<sup>-6</sup> eV/Å. Since the wavefunctions and Kohn-Sham potentials in GPAW are evaluated on a real-space grid [60], a convergence test with respect to this grid spacing is performed and a real-space grid of 0.2 Å is chosen for calculations. The electron-phonon matrix elements are then obtained within the adiabatic approximation using a finite difference technique for evaluating the derivative of the Kohn-Sham potential [68]. Similarly, the momentum matrix elements are calculated using the finite difference technique and the correction terms due to projector augmented waves [69] are added, see Ref. [70]. The width of the Fermi-Dirac occupations is set to  $k_B T = 50$  meV for faster convergence of the DFT results. For generating the Raman spectra, a Gaussian [ $G(\omega) = (\sigma\sqrt{2\pi})^{-1} \exp(-\omega^2/2\sigma^2)$ ] with a variance  $\sigma = 3$  cm<sup>-1</sup> is used to replace the Dirac delta function, which accounts for the inhomogeneous broadening of phonon modes. The temperature of the Bose-Einstein distributions is set to 300 K for all calculations except for the results in top panel of Fig. 7, where a temperature of 77 K is used. The calculations are submitted, managed, and received using the simple MyQueue workflow tool [71], which is a Python front-end to job scheduler.

**Experimental Raman spectra:** The experimental Raman spectra are extracted from the figures in the corresponding references using a common plot digitizer. To remove the noise in the experimental data, they are filtered using a Savitzky-Golay filter [72] of order three with a filter window length of eleven. Furthermore, the Raman moments have been calculated over a frequency range where the main Raman peaks appear, from 350 to 450 cm<sup>-1</sup> for MoS<sub>2</sub> and from 75 to 260 cm<sup>-1</sup> for WTe<sub>2</sub>. For calculating the Euclidean distance, both the experimental and theoretical spectra are convolved with a Gaussian function with variance of 6 cm<sup>-1</sup>. This has been performed to reduce the effect of possible but unimportant small frequency shifts between the experimental and theoretical spectra.

## Acknowledgments

The authors thank M. N. Gjerding for helpful discussions throughout the project. This work was supported by the Center for Nanostructured Graphene (CNG) under the Danish National Research Foundation (project DNRFF103). K. S. T. acknowledges support from the European Research Council (ERC) under the European Unions Horizon 2020 research and innovation program (Grant No. 773122, LIMA).

## References

- [1] K. S. Novoselov, A. K. Geim, S. V. Morozov, D. Jiang, Y. Zhang, S. V. Dubonos, I. V. Grigorieva, and A. A. Firsov, “Electric field effect in atomically thin carbon films”, *Science* **306**, 666–669 (2004).
- [2] B. Anasori, M. R. Lukatskaya, and Y. Gogotsi, “2D metal carbides and nitrides (MXenes) for energy storage”, *Nat. Rev. Mater.* **2**, 16098 (2017).

- [3] X. Xi, L. Zhao, Z. Wang, H. Berger, L. Forró, J. Shan, and K. F. Mak, “Strongly enhanced charge-density-wave order in monolayer NbSe<sub>2</sub>”, *Nat. Nanotechnol.* **10**, 765–769 (2015).
- [4] H. Liu, A. T. Neal, Z. Zhu, Z. Luo, X. Xu, D. Tománek, and P. D. Ye, “Phosphorene: an unexplored 2D semiconductor with a high hole mobility”, *ACS Nano* **8**, 4033–4041 (2014).
- [5] L. Li, Y. Yu, G. J. Ye, Q. Ge, X. Ou, H. Wu, D. Feng, X. H. Chen, and Y. Zhang, “Black phosphorus field-effect transistors”, *Nat. Nanotechnol.* **9**, 372–377 (2014).
- [6] K. F. Mak, C. Lee, J. Hone, J. Shan, and T. F. Heinz, “Atomically thin MoS<sub>2</sub>: a new direct-gap semiconductor”, *Phys. Rev. Lett.* **105**, 136805 (2010).
- [7] Q. H. Wang, K. Kalantar-Zadeh, A. Kis, J. N. Coleman, and M. S. Strano, “Electronics and optoelectronics of two-dimensional transition metal dichalcogenides”, *Nat. Nanotechnol.* **7**, 699–712 (2012).
- [8] L. Ci, L. Song, C. Jin, D. Jariwala, D. Wu, Y. Li, A. Srivastava, Z. F. Wang, K. Storr, L. Balicas, F. Liu, and P. M. Ajayan, “Atomic layers of hybridized boron nitride and graphene domains”, *Nat. Mater.* **9**, 430–435 (2010).
- [9] B. Huang, G. Clark, E. Navarro-Moratalla, D. R. Klein, R. Cheng, K. L. Seyler, D. Zhong, E. Schmidgall, M. A. McGuire, D. H. Cobden, W. Yao, D. Xiao, P. Jarillo-Herrero, and X. Xu, “Layer-dependent ferromagnetism in a van der Waals crystal down to the monolayer limit”, *Nature* **546**, 270–273 (2017).
- [10] H. Wang, X. Huang, J. Lin, J. Cui, Y. Chen, C. Zhu, F. Liu, Q. Zeng, J. Zhou, P. Yu, X. Wang, H. He, S. H. Tsang, W. Gao, K. Suenaga, F. Ma, C. Yang, L. Lu, T. Yu, E. H. T. Teo, G. Liu, and Z. Liu, “High-quality monolayer superconductor NbSe<sub>2</sub> grown by chemical vapour deposition”, *Nat. Commun.* **8**, 394 (2017).
- [11] Y. Cao, V. Fatemi, S. Fang, K. Watanabe, T. Taniguchi, E. Kaxiras, and P. Jarillo-Herrero, “Unconventional superconductivity in magic-angle graphene superlattices”, *Nature* **556**, 43–50 (2018).
- [12] S. Hastrup, M. Strange, M. Pandey, T. Deilmann, P. S. Schmidt, N. F. Hinsche, M. N. Gjerding, D. Torelli, P. M. Larsen, A. C. Riis-Jensen, J. Gath, K. W. Jacobsen, J. J. Mortensen, T. Olsen, and K. S. Thygesen, “The Computational 2D Materials Database: high-throughput modeling and discovery of atomically thin crystals”, *2D Mater.* **5**, 042002 (2018).
- [13] F. Bonaccorso, Z. Sun, T. Hasan, and A. C. Ferrari, “Graphene photonics and optoelectronics”, *Nat. Photon.* **4**, 611–622 (2010).
- [14] K. F. Mak and J. Shan, “Photonics and optoelectronics of 2D semiconductor transition metal dichalcogenides”, *Nat. Photon.* **10**, 216–226 (2016).
- [15] M. N. Gjerding, R. Petersen, T. G. Pedersen, N. A. Mortensen, and K. S. Thygesen, “Layered van der Waals crystals with hyperbolic light dispersion”, *Nat. Commun.* **8**, 320 (2017).
- [16] A. C. Ferrari, “Raman spectroscopy of graphene and graphite: disorder, electron-phonon coupling, doping and nonadiabatic effects”, *Solid State Commun.* **143**, 47–57 (2007).
- [17] A. C. Ferrari and D. M. Basko, “Raman spectroscopy as a versatile tool for studying the properties of graphene”, *Nat. Nanotechnol.* **8**, 235–246 (2013).
- [18] X.-L. Li, W.-P. Han, J.-B. Wu, X.-F. Qiao, J. Zhang, and P.-H. Tan, “Layer-number dependent optical properties of 2D materials and their application for thickness determination”, *Adv. Funct. Mater.* **27**, 1604468 (2017).
- [19] D. A. Long, *The raman effect: a unified treatment of the theory of Raman scattering by molecules* (John Wiley & Sons Ltd, Chichester, 2002).
- [20] C. P. Wilson E.B. Decius J.C., ed., *Molecular vibrations. the theory of infrared and Raman vibrational spectra* (Dover Publications, New York, 1980).
- [21] P. Umari and A. Pasquarello, “First-principles analysis of the Raman spectrum of vitreous silica: comparison with the vibrational density of states”, *J. Phys. Condens. Matter* **15**, S1547–S1552 (2003).
- [22] S. A. Prosandeev, U. Waghmare, I. Levin, and J. Maslar, “First-order Raman spectra of AB<sub>1/2</sub>B<sub>1/2</sub>O<sub>3</sub> double perovskites”, *Phys. Rev. B* **71**, 214307 (2005).
- [23] Q. Liang, S. Dwaraknath, and K. A. Persson, “High-throughput computation and evaluation of Raman spectra”, *Sci. Data* **6**, 135 (2019).

- [24] R. Saito, M. Hofmann, G. Dresselhaus, A. Jorio, and M. S. Dresselhaus, “Raman spectroscopy of graphene and carbon nanotubes”, *Adv. Phys.* **60**, 413–550 (2011).
- [25] Q. Cai, D. Scullion, A. Falin, K. Watanabe, T. Taniguchi, Y. Chen, E. J. G. Santos, and L. H. Li, “Raman signature and phonon dispersion of atomically thin boron nitride”, *Nanoscale* **9**, 3059–3067 (2017).
- [26] Y. C. Jiang, J. Gao, and L. Wang, “Raman fingerprint for semi-metal WTe<sub>2</sub> evolving from bulk to monolayer”, *Sci. Rep.* **6**, 19624 (2016).
- [27] L. Liang and V. Meunier, “First-principles Raman spectra of MoS<sub>2</sub>, WS<sub>2</sub> and their heterostructures”, *Nanoscale* **6**, 5394 (2014).
- [28] A. H. Larsen, M. Vanin, J. J. Mortensen, K. S. Thygesen, and K. W. Jacobsen, “Localized atomic basis set in the projector augmented wave method”, *Phys. Rev. B* **80**, 195112 (2009).
- [29] *The C2DB website*, <https://cmrdb.fysik.dtu.dk/c2db>. Currently the Raman data can be found in this [temporary link](#).
- [30] K. T. Butler, D. W. Davies, H. Cartwright, O. Isayev, and A. Walsh, “Machine learning for molecular and materials science”, *Nature* **559**, 547–555 (2018).
- [31] J. Schmidt, M. R. G. Marques, S. Botti, and M. A. L. Marques, “Recent advances and applications of machine learning in solid-state materials science”, *Npj Comput. Mater.* **5**, 83 (2019).
- [32] A. C. Albrecht, “On the theory of Raman intensities”, *J. Chem. Phys.* **34**, 1476–1484 (1961).
- [33] S.-Y. Lee and E. J. Heller, “Time-dependent theory of Raman scattering”, *J. Chem. Phys.* **71**, 4777 (1979).
- [34] R. Loudon, “Theory of the first-order Raman effect in crystals”, *Proc. R. Soc.* **275**, 218–232 (1963).
- [35] A. K. Ganguly and J. L. Birman, “Theory of lattice Raman scattering in insulators”, *Phys. Rev.* **162**, 806–816 (1967).
- [36] M. Cardona, ed., *Light scattering in solids I* (Springer, Berlin, 1983).
- [37] P. Y. Yu and M. Cardona, *Fundamentals of semiconductors: physics and materials properties* (Springer, Berlin, 2010).
- [38] G. Grosso and G. P. Parravicini, *Solid state physics* (Academic Press, San Diego, California, 2000).
- [39] M. Dresselhaus, G. Dresselhaus, R. Saito, and A. Jorio, “Raman spectroscopy of carbon nanotubes”, *Phys. Rep.* **409**, 47–99 (2005).
- [40] J. Zhang, S. Jia, I. Kholmanov, L. Dong, D. Er, W. Chen, H. Guo, Z. Jin, V. B. Shenoy, L. Shi, and J. Lou, “Janus monolayer transition-metal dichalcogenides”, *ACS Nano* **11**, 8192–8198 (2017).
- [41] B. R. Carvalho, L. M. Malard, J. M. Alves, C. Fantini, and M. A. Pimenta, “Symmetry-dependent exciton-phonon coupling in 2D and bulk MoS<sub>2</sub> observed by resonance Raman scattering”, *Phys. Rev. Lett.* **114**, 136403 (2015).
- [42] N. Scheuschner, R. Gillen, M. Staiger, and J. Maultzsch, “Interlayer resonant Raman modes in few-layer MoS<sub>2</sub>”, *Phys. Rev. B* **91**, 235409 (2015).
- [43] J.-U. Lee, K. Kim, and H. Cheong, “Resonant Raman and photoluminescence spectra of suspended molybdenum disulfide”, *2D Mater.* **2**, 044003 (2015).
- [44] Y. Wang, B. R. Carvalho, and V. H. Crespi, “Strong exciton regulation of Raman scattering in monolayer MoS<sub>2</sub>”, *Phys. Rev. B* **98**, 161405 (2018).
- [45] F. Xia, H. Wang, and Y. Jia, “Rediscovering black phosphorus as an anisotropic layered material for optoelectronics and electronics”, *Nat. Commun.* **5**, 4458 (2014).
- [46] Z. Fei, T. Palomaki, S. Wu, W. Zhao, X. Cai, B. Sun, P. Nguyen, J. Finney, X. Xu, and D. H. Cobden, “Edge conduction in monolayer WTe<sub>2</sub>”, *Nature Physics* **13**, 677–682 (2017).
- [47] H. Li, Q. Zhang, C. C. R. Yap, B. K. Tay, T. H. T. Edwin, A. Olivier, and D. Baillargeat, “From bulk to monolayer MoS<sub>2</sub>: evolution of Raman scattering”, *Adv. Funct. Mater.* **22**, 1385–1390 (2012).
- [48] N. A. Lanzillo, A. G. Birdwell, M. Amani, F. J. Crowne, P. B. Shah, S. Najmaei, Z. Liu, P. M. Ajayan, J. Lou, M. Dubey, S. K. Nayak, and T. P. O’Regan, “Temperature-dependent phonon shifts in monolayer MoS<sub>2</sub>”, *Appl. Phys. Lett.* **103**, 093102 (2013).

- [49] S. Tongay, J. Suh, C. Ataca, W. Fan, A. Luce, J. S. Kang, J. Liu, C. Ko, R. Raghunathanan, J. Zhou, F. Ogletree, J. Li, J. C. Grossman, and J. Wu, “Defects activated photoluminescence in two-dimensional semiconductors: interplay between bound, charged and free excitons”, *Sci. Rep.* **3**, 2657 (2013).
- [50] K. Chen, Z. Chen, X. Wan, Z. Zheng, F. Xie, W. Chen, X. Gui, H. Chen, W. Xie, and J. Xu, “A simple method for synthesis of high-quality millimeter-scale 1T’ transition-metal telluride and near-field nanooptical properties”, *Adv. Mater.* **29**, 1700704 (2017).
- [51] J. Zhou, F. Liu, J. Lin, X. Huang, J. Xia, B. Zhang, Q. Zeng, H. Wang, C. Zhu, L. Niu, X. Wang, W. Fu, P. Yu, T.-R. Chang, C.-H. Hsu, D. Wu, H.-T. Jeng, Y. Huang, H. Lin, Z. Shen, C. Yang, L. Lu, K. Suenaga, W. Zhou, S. T. Pantelides, G. Liu, and Z. Liu, “Large-area and high-quality 2D transition metal telluride”, *Adv. Mater.* **29**, 1603471 (2016).
- [52] Y. Cao, N. Sheremetyeva, L. Liang, H. Yuan, T. Zhong, V. Meunier, and M. Pan, “Anomalous vibrational modes in few layer WTe<sub>2</sub> revealed by polarized Raman scattering and first-principles calculations”, *2D Mater.* **4**, 035024 (2017).
- [53] K. Ghosh, A. Stuke, M. Todorović, P. B. Jørgensen, M. N. Schmidt, A. Vehtari, and P. Rinke, “Deep learning spectroscopy: neural networks for molecular excitation spectra”, *Adv. Sci.* **6**, 1801367 (2019).
- [54] A. Walsh, “The quest for new functionality”, *Nat. Chem.* **7**, 274–275 (2015).
- [55] B. Arnaud, S. Lebegue, P. Rabiller, and M. Alouani, “Huge excitonic effects in layered hexagonal boron nitride”, *Phys. Rev. Lett.* **96**, 026402 (2006).
- [56] P. Cudazzo, L. Sponza, C. Giorgetti, L. Reining, F. Sottile, and M. Gatti, “Exciton band structure in two-dimensional materials”, *Phys. Rev. Lett.* **116**, 066803 (2016).
- [57] A. Taghizadeh and T. G. Pedersen, “Gauge invariance of excitonic linear and nonlinear optical response”, *Phys. Rev. B* **97**, 205432 (2018).
- [58] F. Giustino, “Electron-phonon interactions from first principles”, *Rev. Mod. Phys.* **89**, 015003 (2017).
- [59] A. Taghizadeh, F. Hipolito, and T. G. Pedersen, “Linear and nonlinear optical response of crystals using length and velocity gauges: effect of basis truncation”, *Phys. Rev. B* **96**, 195413 (2017).
- [60] J. J. Mortensen, L. B. Hansen, and K. W. Jacobsen, “Real-space grid implementation of the projector augmented wave method”, *Phys. Rev. B* **71**, 035109 (2005).
- [61] J. Enkovaara, C. Rostgaard, J. J. Mortensen, J. Chen, M. Dułak, L. Ferrighi, J. Gavnholt, C. Glinsvad, V. Haikola, H. A. Hansen, H. H. Kristoffersen, M. Kuisma, A. H. Larsen, L. Lehtovaara, M. Ljungberg, O. Lopez-Acevedo, P. G. Moses, J. Ojanen, T. Olsen, V. Petzold, N. A. Romero, J. Stausholm-Møller, M. Strange, G. A. Tritsarlis, M. Vanin, M. Walter, B. Hammer, H. Häkkinen, G. K. H. Madsen, R. M. Nieminen, J. K. Nørskov, M. Puska, T. T. Rantala, J. Schiøtz, K. S. Thygesen, and K. W. Jacobsen, “Electronic structure calculations with GPAW: a real-space implementation of the projector augmented-wave method”, *J. Condens. Matter Phys.* **22**, 253202 (2010).
- [62] S. Bahn and K. Jacobsen, “An object-oriented scripting interface to a legacy electronic structure code”, *Comput. Sci. Eng.* **4**, 56–66 (2002).
- [63] A. H. Larsen, J. J. Mortensen, J. Blomqvist, I. E. Castelli, R. Christensen, M. Dułak, J. Friis, M. N. Groves, B. Hammer, C. Hargus, E. D. Hermes, P. C. Jennings, P. B. Jensen, J. Kermode, J. R. Kitchin, E. L. Kolsbjerg, J. Kubal, K. Kaasbjerg, S. Lysgaard, J. B. Maronsson, T. Maxson, T. Olsen, L. Pastewka, A. Peterson, C. Rostgaard, J. Schiøtz, O. Schütt, M. Strange, K. S. Thygesen, T. Vegge, L. Vilhelmsen, M. Walter, Z. Zeng, and K. W. Jacobsen, “The atomic simulation environment: a Python library for working with atoms”, *J. Phys. Condens. Matter* **29**, 273002 (2017).
- [64] J. P. Perdew, K. Burke, and M. Ernzerhof, “Generalized gradient approximation made simple”, *Phys. Rev. Lett.* **77**, 3865–3868 (1996).
- [65] J. Fritsch, “Density functional calculation of semiconductor surface phonons”, *Phys. Rep.* **309**, 209–331 (1999).
- [66] J. Sólyom, *Fundamentals of the physics of solids: structure and dynamics*, Vol. 1 (Springer, Berlin, 2007).

- [67] D. Alfè, “PHON: a program to calculate phonons using the small displacement method”, [Comput. Phys. Commun.](#) **180**, 2622–2633 (2009).
- [68] K. Kaasbjerg, K. S. Thygesen, and K. W. Jacobsen, “Phonon-limited mobility in *n*-type single-layer MoS<sub>2</sub> from first principles”, [Phys. Rev. B](#) **85**, 115317 (2012).
- [69] P. E. Blöchl, “Projector augmented-wave method”, [Phys. Rev. B](#) **50**, 17953–17979 (1994).
- [70] J. Yan, J. J. Mortensen, K. W. Jacobsen, and K. S. Thygesen, “Linear density response function in the projector augmented wave method: applications to solids, surfaces, and interfaces”, [Phys. Rev. B](#) **83**, 245122 (2011).
- [71] J. Mortensen, M. Gjerding, and K. Thygesen, “MyQueue: task and workflow scheduling system”, [J. Open Source Softw.](#) **5**, 1844 (2020).
- [72] A. Savitzky and M. J. E. Golay, “Smoothing and differentiation of data by simplified least squares procedures.”, [Anal. Chem.](#) **36**, 1627–1639 (1964).